Laser & Photonics Reviews

LASER & PHOTONICS REVIEWS
www.lpr-journal.org

RESEARCH ARTICLE

Femtosecond Laser Line-Exposure Fabrication of Planar Chiral Microstructures for OAM-Sign Discrimination and Spatial Encoding

Yusheng Jin[1] | Shiyun Zou[1] | Shibo Xu[1] | Yihang Yin[2] | Youdi Hu[1] | Xiaoxu Rao[1] | Feng Tang[1] | Yanlei Hu[1] | Jincheng Ni[1] | Jiawen Li[1] | Dong Wu[1] | Deng Pan[1,2]

[1]State Key Laboratory of Opto-Electronic Information Acquisition and Protection Technology, Department of Precision Machinery and Precision Instrumentation, University of Science and Technology of China, Hefei, China | [2]Information Materials and Intelligent Sensing Laboratory of Anhui Province, School of Optoelectronic Science and Engineering, Anhui University, Hefei, China

Correspondence: Youdi Hu (youdihu@ustc.edu.cn) | Jincheng Ni (njc@ustc.edu.cn) | Deng Pan (pandeng@ahu.edu.cn)

Received: 14 May 2026 | **Revised:** 7 September 2026 | **Accepted:** 11 September 2026

Keywords: femtosecond laser line exposure | OAM-sign discrimination | orbital angular momentum | planar chiral microstructures | spatial light modulation | vortex dichroism

ABSTRACT

Orbital angular momentum (OAM) provides an additional degree of freedom for structured-light information encoding, yet vortex beams with opposite topological charges have nearly identical transverse intensity profiles, making the sign of l difficult to determine by direct intensity detection. Here, a spatial-light-modulator (SLM)-assisted femtosecond laser line-exposure method is developed for programmable fabrication of planar chiral microstructures and arrays. Based on actual processing comparisons, the throughput of the linear exposure per structure is approximately 47.8 times higher than that of point-by-point path writing. Mirror-enantiomeric structures exhibit vortex-dependent differential-reflection responses of opposite sign, converting the OAM phase handedness into a measurable intensity difference, with a reflection-mode vortex dichroism (VD) magnitude reaching approximately 0.25. Using this response, all 100 randomly ordered positive- and negative-OAM inputs are correctly classified under the tested conditions. The concept is further extended to OAM-keyed spatial encoding and optical readout using chiral microstructure arrays. This approach combines programmable microfabrication, planar chiral optics, and OAM-sign readout in an array-compatible platform for structured-light state analysis.

1 | Introduction

Orbital angular momentum (OAM) is a distinct degree of freedom of structured light [1]. A vortex beam carries an azimuthal phase factor $\exp(il\varphi)$, where the sign and magnitude of the topological charge l specify the handedness and winding order of the helical phase, respectively. Alongside conventional degrees of freedom such as polarization and wavelength, OAM provides an additional discrete state space and has been widely explored for high-dimensional optical encoding [2, 3], mode multiplexing [4, 5], quantum information [6, 7], and optical sensing [8]. Reliable vortex generation is now available through spiral phase plates [9], computer-generated holograms [10], metasurfaces [11], and related approaches. The complementary problem of compact, stable, and directly detectable analysis of an incident OAM state remains important for OAM photonic systems [12, 13].

Yusheng Jin and Shiyun Zou contributed equally to this work.

In particular, $+l$ and $-l$ vortex beams with the same $|l|$ have nearly identical transverse intensity distributions under ideal conditions; their distinction is encoded primarily in the opposite azimuthal phase gradients. Direct intensity detection of the incident beam alone therefore does not reveal the OAM sign [14]. A passive optical structure that converts phase handedness into a measurable intensity contrast would provide a simple route to OAM-sign discrimination, state readout, and subsequent spatial information processing.

Chiral light-matter interactions offer a route to such phase-sensitive readout [15, 16]. Because a chiral structure lacks specific mirror symmetries, coupling to +l and −l vortex beams with opposite phase handedness can produce different scattering, reflection, or transmission responses, thereby mapping the OAM sign onto an intensity signal accessible to a detector. Three-dimensional helices [17] and other spatially chiral micro/nanostructures [18–20] have been shown to support pronounced OAM-dependent differential optical responses. Their fabrication, however, often relies on point-by-point three-dimensional scanning [21], multilayer assembly [22], or complex self-organization [23], for which geometric complexity and processing time increase rapidly with array size. OAM-readout arrays require more than a detectable optical contrast; fabrication consistency, programmability, and throughput are also important. Planar chiral structures can be constructed from a small number of two-dimensional geometric elements and are readily arranged into spatial arrays, but efficient programmable fabrication of well-defined mirror-enantiomeric microstructures together with stable OAM-dependent readout remains insufficiently explored.

Femtosecond-laser two-photon polymerization provides substantial three-dimensional fabrication freedom and is widely used to construct chiral microstructures [24, 25]. Conventional point-by-point writing, however, exposes voxels sequentially along a prescribed trajectory. When the target geometry is composed mainly of straight segments, this strategy introduces many repetitive scanning operations and limits the throughput of large arrays. Focal-field shaping with a spatial light modulator (SLM) provides an alternative [26–28]. By transforming the conventional point focus into a line-shaped focus with programmable orientation and length, an entire structural arm can be formed in a single exposure rather than reconstructed point by point [29]. The orientation, length, position, and exposure condition of each line can then be controlled to assemble planar structures with prescribed spatial symmetries. For line-based planar chiral microstructures, this one-line-per-exposure strategy reduces the number of writing operations while retaining programmable geometry, making it well suited to OAM-responsive structural arrays with spatial encoding functionality.

Here, an SLM-assisted femtosecond laser line-exposure method is introduced for rapid fabrication of planar chiral microstructures assembled from linear building blocks. Programmable control of the line-shaped focal field enables mirror-enantiomeric structures and their arrays to be fabricated with defined orientations, lengths, and spatial positions. Relative to point-by-point path writing, a complete structural arm is produced in one stationary exposure, reducing the number of writing steps and increasing array throughput. Full-wave electromagnetic simulations are used to analyze the interaction between vortex beams and planar chiral structures, linking opposite OAM phase winding to non-equivalent coupling and differential reflection from mirror-related geometries. Experimentally, the reflection responses of mirror-enantiomeric structures are measured under opposite topological charges, and 100 randomized +l/−l inputs are used to evaluate binary OAM-sign readout. Chiral unit cells are further extended into spatial arrays for OAM-keyed spatial encoding and optical readout. The resulting framework combines line-exposure fabrication, planar mirror chirality, and OAM-dependent differential reflection in a programmable platform for arrayed OAM-state readout.

2 | Results

2.1 | SLM-Assisted Femtosecond Laser Line-Exposure Strategy

To rapidly fabricate planar microstructures composed of linear building blocks, an SLM-assisted femtosecond laser line-exposure system was constructed (Figure 1a). The femtosecond beam was polarization-conditioned and expanded before impinging on a reflective SLM. A cylindrical-lens phase hologram imposed one-dimensional quadratic phase modulation, and a high-numerical-aperture objective focused the modulated beam into a line-shaped field at the focal plane. During fabrication, this field was positioned at the photoresist/substrate interface to induce two-photon polymerization in SZ2080. Unlike conventional point-by-point writing, in which a point focus is translated continuously to trace a line, the entire line-shaped focal field serves as a single exposure element, allowing one continuous polymerized line to be generated in a stationary exposure.

The shaped focal field was examined numerically and experimentally and then compared with the polymerized structure (Figure 1b). Both the simulated and measured focal distributions in Figure 1 exhibit a clear line-like profile, while a single exposure produces a continuous linear microstructure in SZ2080, as confirmed by scanning electron microscopy (SEM). The line orientation can also be adjusted digitally. Rotating the cylindrical-lens phase pattern on the SLM rotates the line-shaped focus in the sample plane without mechanically rotating the specimen. Together with stage positioning, this provides independent control over the orientation and position of each line exposure, enabling isolated line elements to be assembled into prescribed two-dimensional patterns or arrays. The representative arrays shown on the right side of Figure 1c demonstrate programmable spatial arrangement of line elements over a larger field of view.

The fabrication concept can therefore be summarized as follows: the SLM first converts a conventional point focus into a programmable line-shaped exposure element; digital field control and stage positioning then assemble these line elements into two-dimensional microstructures. This line-element-by-line-element strategy is particularly suited to the planar chiral structures used below, because each structural arm can be mapped directly onto one line exposure, reducing the repeated path scanning required in point-wise writing.

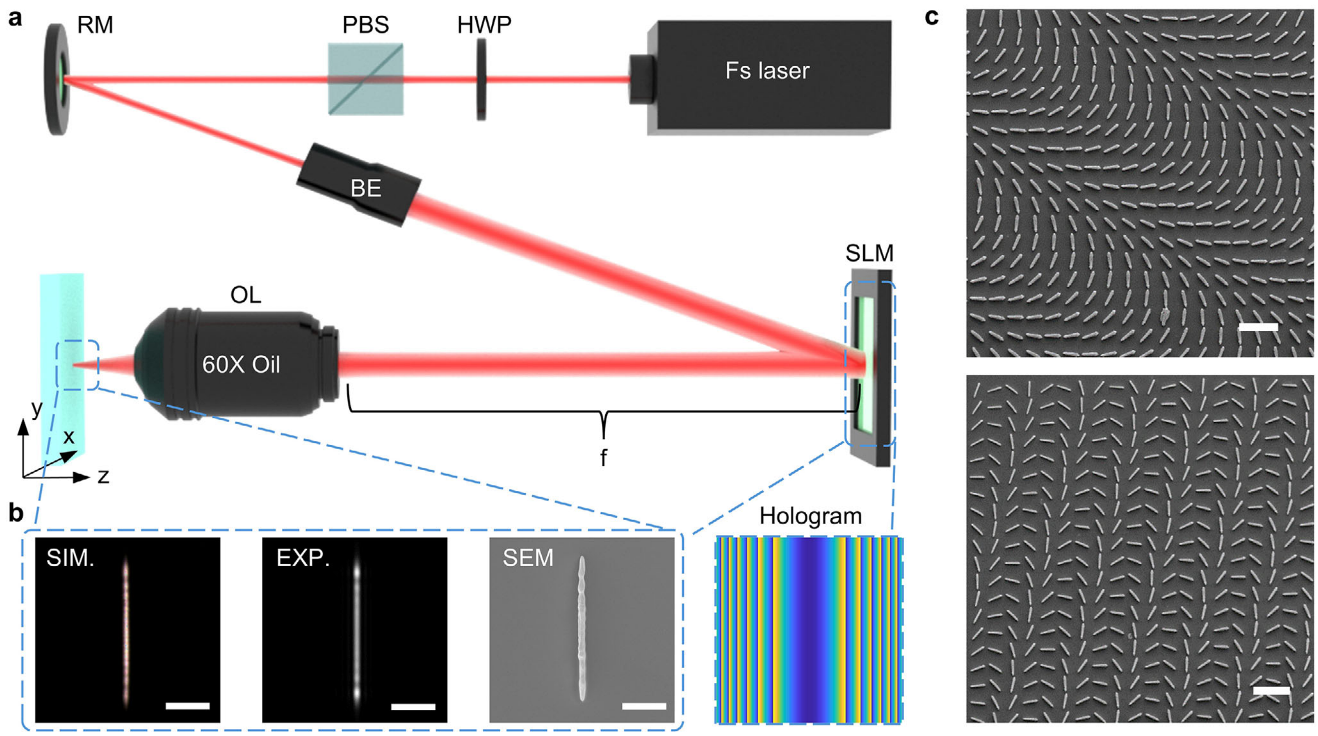

FIGURE 1 | SLM-assisted femtosecond laser line-exposure fabrication and programmable assembly of line elements. (a) Schematic of the femtosecond laser line-exposure system. The incident femtosecond beam is conditioned and phase-modulated by a reflective SLM, then focused by a 60× oil-immersion high-numerical-aperture objective to form a line-shaped focal field in the photoresist. RM, reflecting mirror; PBS, polarizing beam splitter; HWP, half-wave plate; BE, beam expander; OL, objective lens. (b) Formation and fabrication validation of the line-shaped exposure element, including the simulated line focus (SIM.), experimentally measured focal distribution (EXP.), and an SEM image of a polymerized line generated by a single exposure (SEM). A representative cylindrical-lens phase hologram loaded on the SLM is shown on the right. (c) Representative two-dimensional arrays assembled from line-shaped exposure elements with different spatial orientations, demonstrating programmable spatial assembly through SLM hologram control and stage positioning. Scale bar: 5 μm in (b); 20 μm in (c).

2.2 | Programmable Geometric Control and High-Throughput Fabrication of Line-Based Planar Microstructures

After establishing the line-exposure strategy, the geometric controllability of an individual line element and its scalability toward more complex planar structures were evaluated (Figure 2). For line-based microstructures, length, width, orientation, and spatial position define the final geometry. We therefore first examined how the SLM hologram parameters and laser exposure conditions control the dimensions of the polymerized lines.

As shown in Figure 2a, with the remaining exposure conditions fixed, changing the effective lateral extent of the cylindrical-lens phase region on the SLM continuously modifies the longitudinal extent of the line-shaped focal field and, in turn, the length of the polymerized line. Reducing the effective modulation size shortens the fabricated structure. Over the investigated range, the measured line length varies approximately linearly with the programmed hologram parameter, indicating that the longitudinal dimension can be controlled digitally without changing the mechanical scan trajectory.

With the line-field length held fixed, the incident average laser power was varied to control the polymerized linewidth (Figure 2b). The linewidth increases with laser power, whereas the overall line length changes comparatively little. This behavior is consistent with the threshold nature of two-photon polymerization: at higher exposure levels, a broader transverse region of the focal field exceeds the polymerization threshold [30]. To describe the femtosecond exposure conditions more completely, the corresponding pulse energy and effective peak intensity were estimated from the average power, repetition rate, and pulse duration (Section S1).

Atomic force microscopy (AFM) was used to characterize the three-dimensional morphology of a representative polymerized line (Figure 2c). The surface profile shows a continuous ridge with a well-defined cross-section, while transverse and longitudinal traces provide the linewidth and height information. These measurements confirm that the line-shaped focal field produces a continuous three-dimensional polymerized feature suitable for assembling planar functional structures from multiple line exposures.

Once the individual line element was controlled, more complex patterns were constructed by sequentially loading holograms with different sizes and orientations while positioning the sample stage according to the prescribed geometry. The numbers, triangles, squares, and other line-based two-dimensional motifs in Figure 2d can all be generated with a finite number of line exposures. These patterns are included to demonstrate general

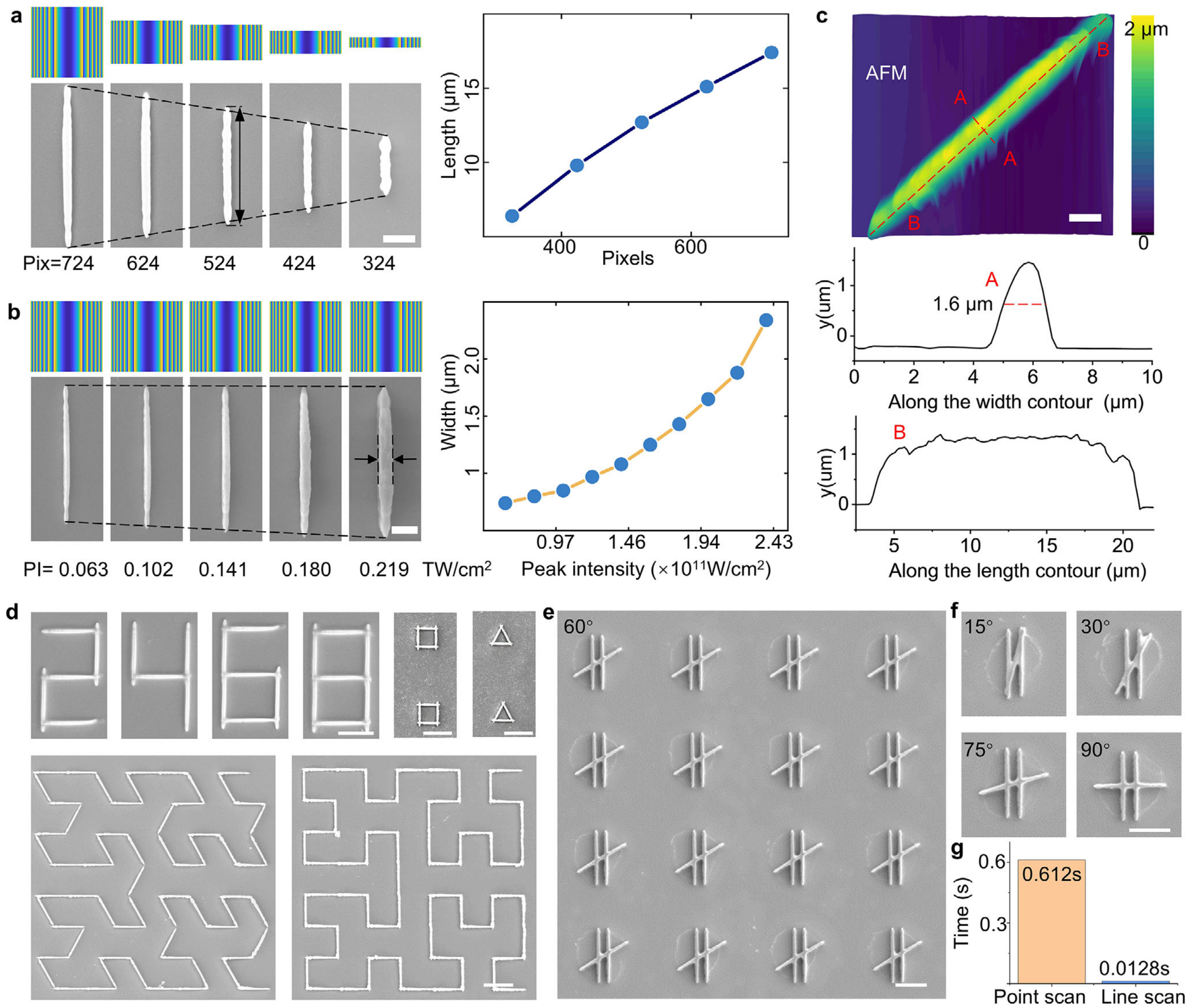

FIGURE 2 | Programmable geometric control and fabrication of line-based planar microstructures. (a) Control of polymerized line length by changing the effective modulation size of the cylindrical-lens phase hologram on the SLM (estimated effective peak intensity 0.141 TW/cm^2 and exposure time of 0.5 s); representative holograms and corresponding SEM images are shown on the left, and the measured line length is plotted against the programmed parameter on the right. (b) Control of linewidth by varying the average laser power at fixed hologram size and exposure time (0.5 s); SEM images acquired under different exposure conditions are shown on the left, and the linewidth is plotted as a function of exposure level on the right. The corresponding peak intensity I_peak is an estimate based on the pulse parameters and effective exposure dimensions. (c) AFM topography of a representative polymerized line and transverse/longitudinal cross-sectional profiles. (d) Representative two-dimensional patterns assembled from programmable line exposures, including numbers, polygons, and other line-based motifs. (e) Array of representative planar chiral structures assembled from three line exposures. (f) Structures fabricated with different programmed inclination angles (defined with respect to the y-axis), used to verify orientation programmability. (g) Comparison of the processing time per structure for point-by-point path writing and line exposure under the present experimental configuration. Scale bars: 3 μm in (a, b); 2 μm in (c); 10 μm in (d, e, f).

geometric assembly across different line counts, orientations, and connection schemes rather than to imply a specific optical function.

The same assembly strategy was then applied to the N-shaped planar chiral structures used in the vortex-optics experiments. Each functional unit comprises two approximately parallel vertical arms connected by an inclined arm and can therefore be decomposed into three line exposures. Figure 2e shows an array of representative structures, and Figure 2f presents units fabricated with several programmed inclination angles. Statistical characterization confirms good within-batch reproducibility (Section S2). The orientation of the inclined arm is changed by digitally rotating the phase hologram, without rotating the sample.

The throughput advantage follows directly from the one-line-per-arm exposure scheme. Point-by-point writing requires continuous scanning along each structural path, whereas line exposure forms a complete arm in one stationary exposure and therefore reduces the number of writing and positioning operations for structures composed of only a few straight segments. Under a unified timing definition and the present experimental configuration, point-by-point path writing requires approximately 0.612 s per structure, compared with approximately 0.0128 s per structure for line exposure (Figure 2g and Section S3), corresponding to a throughput enhancement of about 47.8-fold. Figures 1 and 2 thus establish the fabrication pathway from line-field generation and geometric control to rapid construction of planar chiral functional units.

2.3 | Vortex-Dependent Differential Reflection From N-Shaped Planar Chiral Structures

To investigate OAM-sign-sensitive optical responses, a pair of planar functional structures related by in-plane mirror reflection was selected (Figure 3). The two geometries are referred to as right-handed and left-handed planar structures. The incident vortex field in polar coordinate space can be described as:

$$E_{source} = C\frac{r^{|l|}}{\sqrt{|l|!}}e^{-\frac{r^2}{w_0^2}}e^{il\varphi} \tag{1}$$

where l is the topological charge, w_0 is the beam waist, and C is a normalized constant independent of l and r. Reversing l from $+l$ to $-l$ reverses the azimuthal phase winding while leaving the ideal transverse intensity distribution $|E|^2$ essentially unchanged. Opposite signs with the same $|l|$ are therefore difficult to distinguish by direct intensity detection of the incident beam; their principal distinction lies in the reversed azimuthal phase gradient.

The planar chiral structure provides a spatial coupling element that converts this difference in phase handedness into an intensity response. Because the line-based geometry lacks the relevant in-plane mirror symmetry, its constituent segments sample the incident vortex phase in a non-equivalent manner. Reversing the topological-charge sign changes the relative phases experienced by different parts of the structure and thereby modifies the local field distribution, scattering interference, and power directed into the reflection channel (Figure 3a). In-plane mirror inversion reverses the geometric handedness and is therefore expected to reverse the sign of the differential response. This mirror inversion–response sign reversal constitutes the central structure–response relation examined in this work.

Full-wave electromagnetic simulations were used to visualize the spatial origin of this differential response. Because SZ2080 exhibits very weak absorption at the working wavelength of 532 nm, it was modeled with a refractive index of $n = 1.6$ and no imaginary component in the simulations [31]. Figure 3b illustrates the right- and left-handed structures under opposite OAM signs together with a representative incident vortex field. Although +l and −l have the same ring-shaped incident intensity distribution, the electromagnetic fields around the structure and at the detection plane differ after interaction. The simulated near-/scattered-field maps in Figure 3c compare the representative structure under +l and −l illumination and include a differential map between the two cases. Distinct local-field enhancement and scattering distributions arise around the constituent line elements, while the mirror structure gives the complementary response. These results support the interpretation that the measured differential reflection originates from non-equivalent coupling between the OAM phase winding and the planar chiral geometry rather than from a difference in the incident intensity profile itself. The sensitivity of this coupling to structural geometry is further analyzed numerically in Section S4.

Experimentally, the directly measured observable is the reflected signal collected under a fixed optical geometry. We therefore describe the response as vortex-dependent differential reflection and define a normalized reflection-mode vortex-dichroism (VD) metric as:

$$VD = \frac{R_{+l} - R_{-l}}{R_{+l,max} + R_{-l,max}} \tag{2}$$

where R_{+l} and R_{-l} denote the normalized reflected signals measured for opposite topological charges of equal magnitude.

Figure 3d compares the reflection responses and the corresponding vortex dichroism spectra of the two mirror-enantiomeric structures. The right- and left-handed geometries exhibit approximately sign-reversed VD responses (maximum VD up to approximately 0.25), consistent with the reversal of the coupling relation under mirror inversion. The complementary response of the two structures provides the physical basis for the OAM-sign readout demonstrated in the next section.

Because SZ2080 is weakly absorbing at the measurement wavelength, the differential response should not be interpreted as conventional absorption dichroism. A more appropriate picture is that opposite OAM signs couple differently to a predominantly refractive microstructure, redistributing optical power among reflection, transmission, and other scattering channels. The present experiments monitor the reflection channel; accordingly, the reported VD describes an OAM-sign-dependent asymmetry in reflection rather than differential material absorption.

In summary, planar mirror chirality converts a difference that is encoded primarily in the OAM phase winding into a measurable differential-reflection signal. The sign reversal between mirror structures further links the response to structural handedness and provides the basis for the OAM-sign discrimination and spatial-encoding experiments that follow.

2.4 | Randomized OAM-Sign Discrimination and OAM-Keyed Spatial Readout

Building on the mirror-chirality-dependent differential reflection established above, we next tested whether the response can serve as a stable intensity-domain readout signal. For a given planar chiral structure, opposite topological charges produce different reflected intensities, while mirror inversion of the structure reverses the high/low response relation (Figure 4a). The combination of structural handedness and OAM sign can therefore be mapped onto two distinguishable intensity states, providing a simple binary readout rule.

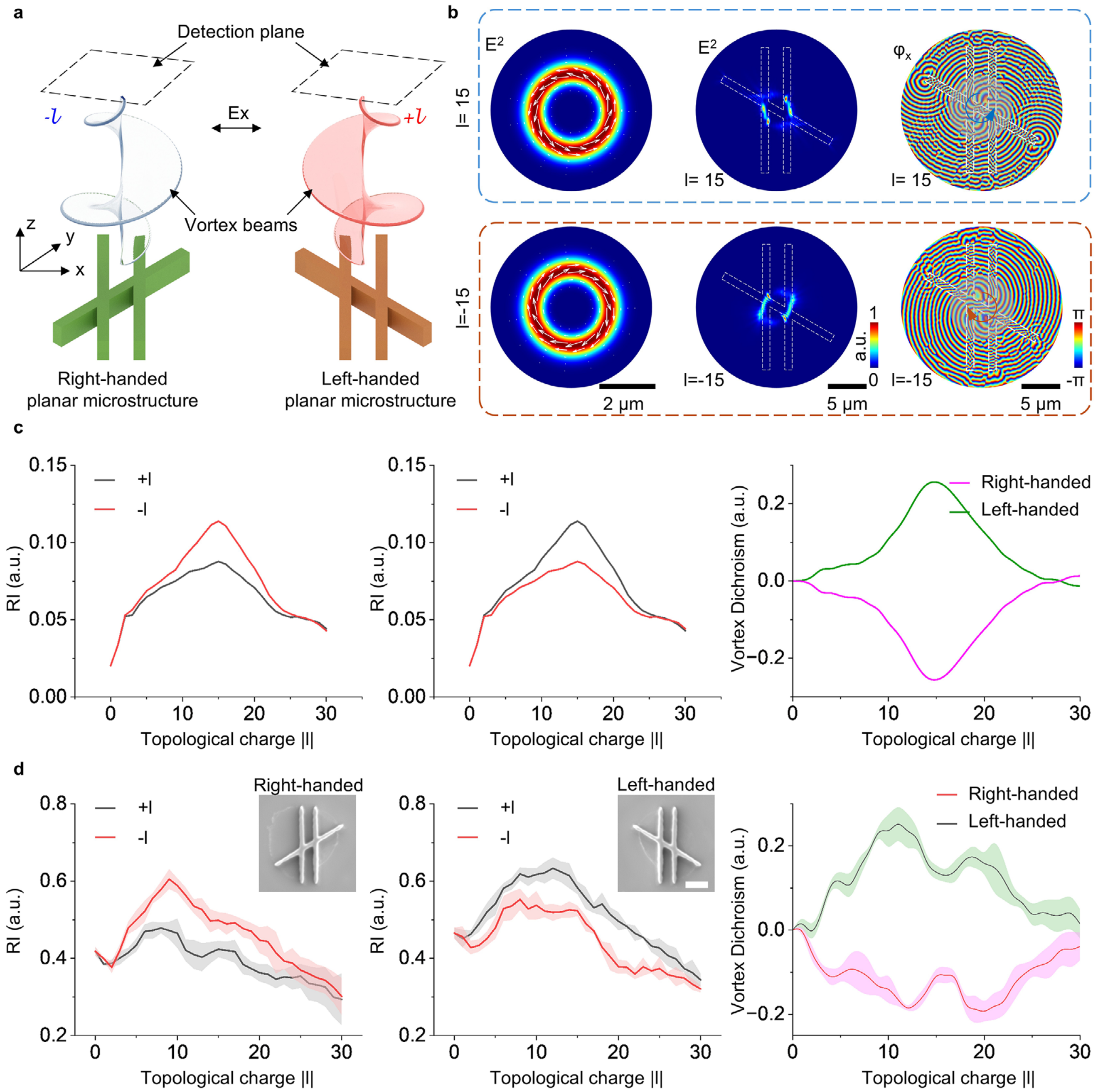

FIGURE 3 | Vortex-dependent differential reflection from N-shaped planar chiral structures. (a) Schematic of right- and left-handed planar structures illuminated by vortex beams with opposite topological charges; the detection plane is located above the structures. (b) Representative simulation results of the coupling between vortex light and planar structures. (c) FDTD-calculated normalized reflection responses of the right- and left-handed structures and the corresponding reflection-mode vortex dichroism (VD) spectra for $l = 0, \pm 1, \ldots, \pm 30$. (d) Experimentally measured normalized reflection responses and corresponding VD spectra. The approximately sign-reversed differential responses show that planar mirror handedness determines the sign of the Orbital angular momentum (OAM)-dependent reflection asymmetry. The reported results represent the mean of the three measurements, with the corresponding standard deviations shown as error bars. Scale bar: 5 μm in (d).

The higher and lower reflected signals are assigned to binary states 1 and 0, respectively. For the right- and left-handed structures, the same OAM sign produces complementary binary outputs; conversely, reversing the OAM sign for a fixed handedness flips the output state. If $s = \pm 1$ denotes the incident OAM sign and $\chi = \pm 1$ denotes the structural handedness, the binary response in Figure 4a is determined by their relative handedness. This mapping converts information encoded in the azimuthal phase winding into an intensity state that can be read directly by a charge-coupled device (CCD) camera (Figure 4b).

Readout repeatability was evaluated using 100 randomized OAM-sign inputs, with 50 $+l$ and 50 $-l$ states. The optical alignment, acquisition conditions, and signal-extraction procedure were kept fixed while the reflected signal was recorded for each input. As shown in Figure 4c, the two classes form clearly separated inten-

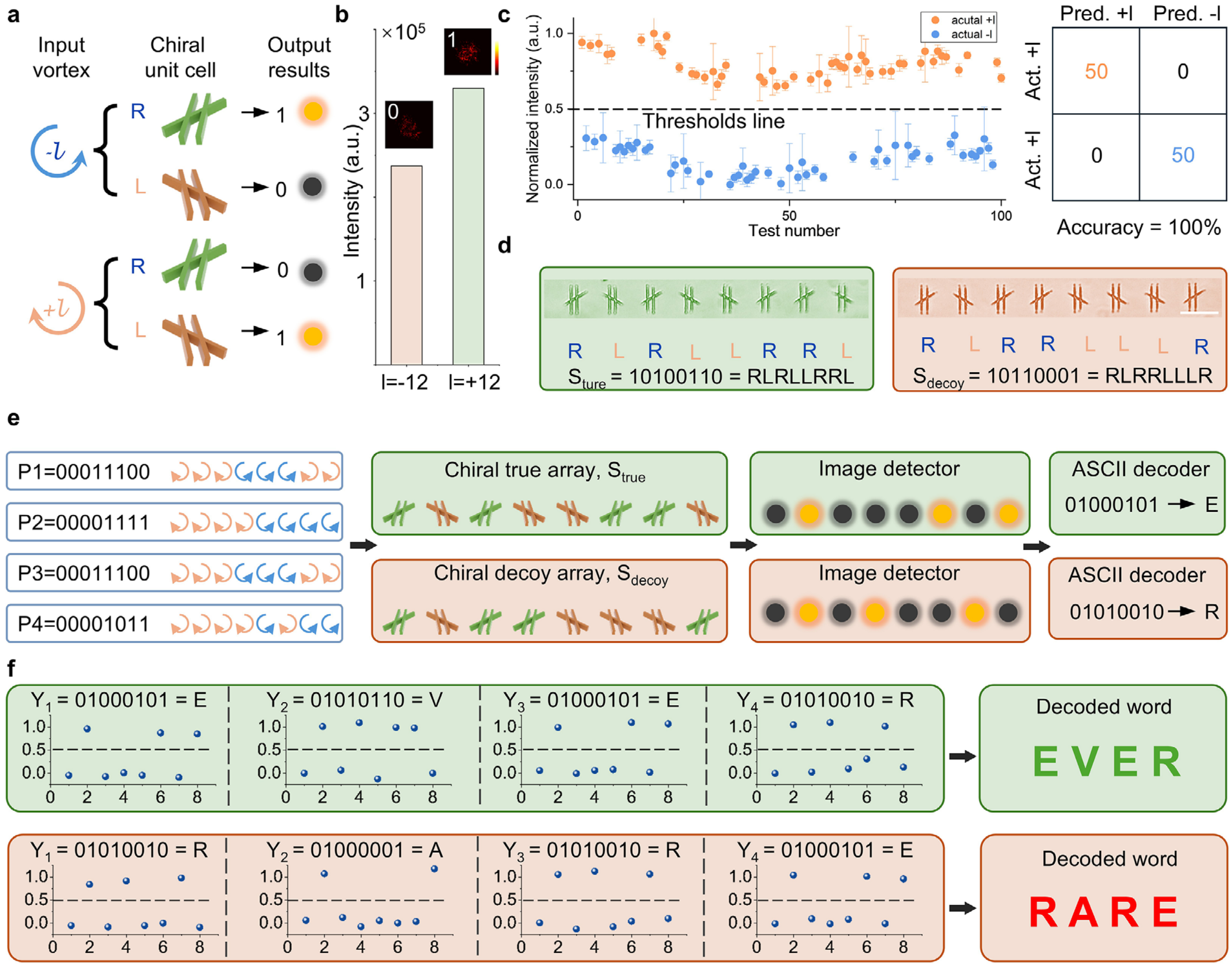

FIGURE 4 | Randomized OAM-sign readout and OAM-keyed spatial encoding using planar chiral microstructure arrays. (a) Binary readout principle based on differential reflection from mirror-enantiomeric structures under opposite OAM signs. For a fixed handedness, +l and −l illumination produce complementary high/low reflected states; mirror inversion reverses this mapping. High and low signals are assigned to binary states 1 and 0, respectively. (b) Representative high- and low-reflection readout states. (c) Extracted signals for 100 randomized OAM inputs, including 50 +l and 50 −l states. The two classes lie on opposite sides of a common decision threshold; the confusion matrix shows that all 100 inputs are classified correctly, corresponding to an observed accuracy of 100% (100/100) under the tested conditions. (d) Target array S_{true} and decoy array S_{decoy} formed by prescribed sequences of right- and left-handed structural elements. (e) OAM-keyed spatial readout and ASCII decoding workflow. Prescribed positive/negative OAM sequences are applied to the structural array, the reflected signals are recorded by a CCD and thresholded into eight-bit binary outputs, and the resulting strings are mapped to ASCII characters. (f) Experimental outputs from four readout sequences. The target array recovers E, V, E, and R to form "EVER", whereas the decoy array recovers R, A, R, and E to form "RARE".

sity populations. Using a single decision threshold, all 50 +l states and all 50 −l states are assigned correctly, giving an observed classification accuracy of 100% (100/100) under the tested conditions. The randomized sequence therefore demonstrates that the differential reflection can function as a binary readout signal beyond ensemble-averaged spectral measurements.

The binary response was then extended from an individual unit to a spatial array. As shown in Figure 4d, right- and left-handed elements were arranged in prescribed sequences to form a target array S_{true} and a decoy array S_{decoy}. In the encoding scheme, structural handedness provides one binary sequence, while a sequence of +l and −l vortex states acts as the optical readout key. The output at each spatial position depends on the local combination of structural handedness and incident OAM sign; the same OAM readout sequence can therefore produce different binary outputs from different chiral arrays.

During each readout operation, a prescribed eight-bit OAM-sign sequence is applied sequentially to the corresponding structural elements (Figure 4e). The image detector records the reflected intensity at each position. Applying the same high/low criterion used for the single-unit measurements converts the optical outputs into an eight-bit binary string, which is then mapped to an ASCII character. Because the target and decoy arrays carry different spatial distributions of handedness, the same readout procedure yields different characters.

Using four prescribed OAM readout sequences, the target array produces the binary outputs 01000101, 01010110, 01000101, and 01010010, corresponding to the ASCII characters E, V, E, and

R. The decoy array instead recovers R, A, R, and E, giving the word "RARE" (Figure 4f). These results show that the OAM-sign-dependent response can be extended from a single readout element to spatially distributed information mapping, providing a proof of concept for OAM-keyed spatial encoding and optical readout.

3 | Discussion

This work combines SLM-assisted femtosecond laser line exposure with planar-chiral OAM readout. A programmable line-shaped focal field serves directly as the elementary writing unit, allowing each structural arm to be formed in a single exposure and assembled into two-dimensional functional geometries by hologram control and stage positioning. Under the present experimental configuration, this approach increases the fabrication throughput per structure by approximately 47.8-fold relative to point-by-point path writing. Optically, the measured OAM-dependent differential reflection arises from non-equivalent coupling between the vortex phase winding and the planar chiral geometry. For +l and −l beams with the same |l|, the transverse intensity distributions are nearly identical, but the azimuthal phase gradients are opposite. Reversing the OAM sign changes the relative excitation phase and scattering interference across the structure, leading to different reflected outputs. The approximately sign-reversed VD responses of the mirror-enantiomeric pair identify mirror-handedness reversal as the primary structure–response relation. In this context, VD describes an OAM-dependent asymmetry in the reflection channel rather than conventional differential absorption.

The resulting phase-to-intensity conversion enables the planar chiral structures to function as passive OAM-sign readout elements. All 100 randomized +l/−l inputs are correctly classified under the tested conditions, and extending mirror-handed elements into spatial arrays enables a combined mapping of OAM readout key, structural-handedness sequence, and binary intensity output. The resulting OAM-keyed spatial encoding and optical readout constitute a proof of concept for arrayed information mapping. However, the present study is limited to representative mirror structures and binary OAM-sign discrimination; accurate recognition of general multimode OAM states will require further investigation.

Overall, programmable line exposure provides an efficient route to planar chiral functional structures, while their OAM-dependent differential reflection supports arrayed OAM-sign readout and spatial information mapping. The combination offers a compact, array-compatible planar platform for structured-light state analysis.

4 | Experimental Section/Methods

4.1 | Femtosecond Laser Direct Writing System

A Ti:sapphire femtosecond laser oscillator (Mai Tai HP, Spectra-Physics) was used as the light source, with a central wavelength of 800 nm, a pulse duration of 100 fs, and a repetition rate of 75 MHz. The polarization state of the laser beam was adjusted by a half-wave plate, and the laser power was controlled using an attenuator. The beam diameter was then adjusted by a beam-expanding system to meet the requirement of subsequent spatial light modulation. The beam was directed onto a reflective phase-only spatial light modulator (SLM, X13138-02, Hamamatsu), which is based on silicon liquid-crystal technology and has a resolution of 1280 × 1024 pixels, a pixel pitch of 12.5 µm, and a refresh rate of 60 Hz. By loading predesigned phase holograms onto the SLM, the wavefront of the incident laser beam was modulated to generate the required optical field distribution. The modulated beam was then focused onto the sample through a 60× oil-immersion objective lens with a numerical aperture of 1.35 for femtosecond laser two-photon polymerization. The sample was mounted on a computer-controlled three-dimensional translation stage to enable programmable fabrication. By changing the holograms loaded onto the SLM, the optical field distribution at the focal plane could be adjusted as required.

4.2 | Hologram Generation and Loading

The cylindrical-lens phase hologram was numerically generated in MATLAB according to the phase function $\Phi(x, y) = \frac{2\pi x^2}{2\lambda f}$, where λ is the laser wavelength and f is the focal length of the cylindrical lens. In the present work, $\lambda = 800$ nm was used, and the phase distribution was discretized according to the pixel pitch of the spatial light modulator (12.5 µm). The cylindrical phase was loaded within a selected central region of the SLM, while the remaining area was left unchanged. By adjusting the lateral size of the loaded phase region, the length of the generated line-shaped focal spot could be tuned. To obtain line-shaped focal spots with different orientations, the cylindrical phase pattern was numerically rotated before being loaded onto the SLM. In addition, a blazed grating phase was superimposed on the hologram to control the diffraction order and spatially separate the desired modulated beam from the undesired orders. The resulting phase pattern was wrapped into the range from 0 to 2π, converted into an 8-bit grayscale hologram, and then loaded onto the SLM *for experimental modulation*.

4.3 | Sample Preparation and Development

A negative photoresist, SZ2080, was used as the fabrication material because of its good optical transparency, mechanical stability, and suitability for femtosecond laser polymerization. Glass coverslips with a size of 20 mm × 20 mm were used as substrates. Before use, the substrates were sequentially cleaned in acetone, ethanol, and deionized water by ultrasonic treatment, and then dried with nitrogen. Approximately 4 µL of photoresist was drop-cast onto the substrate surface to form a thin film, followed by prebaking on a hot plate at 100°C for 60 min to remove residual solvent and stabilize the photoresist layer.

After prebaking, the sample was fixed in an inverted configuration on the sample stage of the femtosecond laser direct writing system. A permanent-magnet fixture was used to maintain stable positioning of the sample during processing. Cedar oil was introduced between the objective lens and the substrate as the refractive-index-matching liquid. The focal position along the z direction was adjusted using a piezoelectric nanopositioning stage so that the line-shaped focal spot generated by the spatial light modulator was focused at the photoresist–glass interface. The designed structures were then written by single-exposure line patterning without point-by-point scanning.

After laser exposure, residual oil on the sample surface was gently removed using a cotton swab wetted with absolute ethanol. The sample was then immersed in n-propanol for 40–60 min to remove the unpolymerized photoresist. After development, the sample was dried gradually in air with the relative humidity controlled below 30%.

4.4 | Characterization and Measurement

The fabricated microstructures were characterized by SEM and AFM to evaluate their morphology and three-dimensional profiles. For the optical measurements, a supercontinuum laser (EU-15, NKT Photonics) was used as the illumination source, and the measurement wavelength was set to 532 nm. The beam was modulated using a spatial light modulator (X15213, Hamamatsu Photonics), with an operating wavelength range of 400–700 nm, to generate vortex beams with topological charges ranging from $l = \pm 1$ to $l = \pm 30$. The incident vortex beam was linearly polarized along the x direction and normally incident on the planar chiral structures. The beam center was aligned with the center of the measured structure, and the reflected signal was collected. For each topological charge, the reflected intensity was obtained by integrating the signal within a fixed region of interest on the recorded image and averaging at least 30 consecutive measurements to suppress short-term intensity fluctuations. The dark-field signal recorded without incident illumination was subtracted from all measurements.

For the measurements in Figure 3, three independent measurements were performed. Before each measurement, the vortex beam was refocused, and its center was realigned with the center of the measured structure. The mirror-enantiomeric structures were fabricated on the same glass substrate and measured under identical experimental conditions.

For the readout experiments in Figure 4, the reflected intensities of each structure under vortex beams with topological charges of $l = +12$ and $l = -12$ were first measured as calibration signals. For each structure, the higher and lower reflected intensities were normalized to 1 and 0, respectively, according to:

$$R_{norm} = \frac{\mathrm{R} - R_{low}}{R_{high} - R_{\mathrm{low}}}$$

where $\mathrm{R_{high}}$ and $\mathrm{R_{low}}$ denote the higher and lower calibration intensities. Accordingly, $\mathrm{R_{norm}} = 0.5$, corresponding to the midpoint between the two calibration signals, was used as the decision threshold for binary readout. The same structure-specific normalization and threshold were then applied to the randomized OAM-sign inputs and the spatial-array readout experiments.

Author Contributions

Y.S.J., S.Y.Z., D.P., and Y.L.H. designed the experiments. S.Y.Z. and D.P. fabricated the samples. Y.S.J., S.Y.Z., Y.H.Y., and S.B.X. performed and analyzed VD intensity measurements. Y.S.J., S.Y.Z., S.B.X., X.X.R., F.T., and D.P. prepared the manuscript. Y.L.H., Y.D.H., J.C.N., J.W.L. and W.D. reviewed and revised the manuscript.

Acknowledgements

This work was funded by the National Key Research and Development Program of China (2024YFB4610700); the National Natural Science Foundation of China (62325507, 52375582, 62205236, 62461160305, 62475066, and 62375253); the Scientific Research Project of Anhui Provincial Department of Education (2024AH050067). We acknowledge the Experimental Center of Engineering and Material Sciences at USTC for the fabrication and measurement of samples. This work was partially carried out at the USTC Center for Micro and Nanoscale Research and Fabrication and Instruments Center for Physical Science, University of Science and Technology of China.

Conflicts of Interest

The authors declare no conflicts of interest.

Data Availability Statement

The data that support the findings of this study are available from the corresponding author upon reasonable request.

References

1. Y. Shen, X. Wang, Z. Xie, et al., "Optical Vortices 30 Years On: OAM Manipulation From Topological Charge to Multiple Singularities," *Light: Science & Applications* 8 (2019): 90, https://doi.org/10.1038/s41377-019-0194-2.

2. X. Ouyang, Y. Xu, M. Xian, et al., "Synthetic Helical Dichroism for Six-Dimensional Optical Orbital Angular Momentum Multiplexing," *Nature Photonics* 15 (2021): 901–907, https://doi.org/10.1038/s41566-021-00880-1.

3. X. Gao, Z. Yu, J. Yao, et al., "Discontinuous Orbital Angular Momentum Metasurface Holography," *Nature Communications* 16 (2025): 10688, https://doi.org/10.1038/s41467-025-65722-y.

4. Z. Liu, S. Gao, Z. Lai, et al., "Broadband, Low-Crosstalk, and Massive-Channels OAM Modes De/Multiplexing Based on Optical Diffraction Neural Network," *Laser & Photonics Reviews* 17 (2023): 2200536.

5. F. Feng, X. Li, Z. Zhang, J. Gan, and X. Yuan, "High-Speed All-Optical Neural Networks Empowered Spatiotemporal Mode Multiplexing," *Light: Science & Applications* 14 (2025): 342, https://doi.org/10.1038/s41377-025-02007-5.

6. Y. Lou, Y. Lv, J. Wang, S. Liu, and J. Jing, "Orbital Angular Momentum Multiplexed Deterministic All-Optical Quantum Erasure-Correcting Code," *Physical Review Letters* 132 (2024): 040601, https://doi.org/10.1103/PhysRevLett.132.040601.

7. W. K. Yu, Q. Y. Wu, X. X. Chen, et al., "Experimental First-Photon Visualization of Quantum Erasure With Hybrid Entanglement," *Laser & Photonics Reviews* 20 (2025): 01816.

8. K. Wang, J. Cheng, Z. Wu, S. Lan, and C. Wan, "Spatiotemporal Doppler Effect," *Laser & Photonics Reviews* (2026): e71442, https://doi.org/10.1002/lpor.71442.

9. E. Brasselet, M. Malinauskas, A. Žukauskas, and S. Juodkazis, "Photopolymerized Microscopic Vortex Beam Generators: Precise Delivery of Optical Orbital Angular Momentum," *Applied Physics Letters* 97 (2010): 211108, https://doi.org/10.1063/1.3517519.

10. F. Shen, W. Fan, Y. Zhang, X. Chen, and Y. Chen, "3D Orbital Angular Momentum Nonlinear Holography," *Advanced Optical Materials* 13 (2025): 2402836.

11. H. Sroor, Y.-W. Huang, B. Sephton, et al., "High-Purity Orbital Angular Momentum States From a Visible Metasurface Laser," *Nature Photonics* 14 (2020): 498–503, https://doi.org/10.1038/s41566-020-0623-z.

12. M. Dai, C. Wang, F. Sun, and Q. J. Wang, "On-Chip Photodetection of Angular Momentums of Vortex Structured Light," *Nature Communications* 15 (2024): 5396, https://doi.org/10.1038/s41467-024-49855-0.

13. J. Ni, C. Huang, L. M. Zhou, et al., "Multidimensional Phase Singularities in Nanophotonics," *Science* 374 (2021): abj0039, https://doi.org/10.1126/science.abj0039.

14. J. Pinnell, V. Rodriguez-Fajardo, and A. Forbes, "How Perfect are Perfect Vortex Beams?," *Optics Letters* 44 (2019): 5614, https://doi.org/10.1364/OL.44.005614.

15. A. Lininger, G. Palermo, A. Guglielmelli, et al., "Chirality in Light–Matter Interaction," *Advanced Materials* 35 (2023): 2107325, https://doi.org/10.1002/adma.202107325.

16. W. Brullot, M. K. Vanbel, T. Swusten, and T. Verbiest, "Resolving Enantiomers Using the Optical Angular Momentum of Twisted Light," *Science Advances* 2 (2016): 1501349.

17. J. Ni, S. Liu, D. Wu, et al., "Gigantic Vortical Differential Scattering as a Monochromatic Probe for Multiscale Chiral Structures," *Proceedings of the National Academy of Sciences* 118 (2021): 2020055118.

18. J. Ni, S. Liu, G. Hu, et al., "Giant Helical Dichroism of Single Chiral Nanostructures With Photonic Orbital Angular Momentum," *ACS Nano* 15 (2021): 2893–2900, https://doi.org/10.1021/acsnano.0c08941.

19. P. Chen, L. L. Ma, W. Hu, et al., "Chirality Invertible Superstructure Mediated Active Planar Optics," *Nature Communications* 10 (2019): 2518, https://doi.org/10.1038/s41467-019-10538-w.

20. J. Li, J. Yan, L. Jiang, and L. Qu, "Chiral Lithography With Vortex Non-Diffracted Laser for Orbital Angular Momentum Detection," *Laser & Photonics Reviews* 18 (2024): 2301050.

21. S. Liu, X. Wang, J. Ni, et al., "Optical Encryption in the Photonic Orbital Angular Momentum Dimension via Direct-Laser-Writing 3D Chiral Metahelices," *Nano Letters* 23 (2023): 2304–2311, https://doi.org/10.1021/acs.nanolett.2c04860.

22. S. Liu, J. Ni, C. Zhang, et al., *Laser & Photonics Reviews* 16 (2022): 2100518, https://doi.org/10.1002/lpor.202100518.

23. Y. Hu, H. Yuan, S. Liu, et al., "Chiral Assemblies of Laser-Printed Micropillars Directed by Asymmetrical Capillary Force," *Advanced Materials* 32 (2020): 2002356, https://doi.org/10.1002/adma.202002356.

24. A. Jaiswal, C. K. Rastogi, S. Rani, G. P. Singh, S. Saxena, and S. Shukla, "Two Decades of Two-Photon Lithography: Materials Science Perspective for Additive Manufacturing of 2D/3D Nano-Microstructures," *Iscience* 26 (2023): 106374, https://doi.org/10.1016/j.isci.2023.106374.

25. J. Wang, Z. Shang, S. Sun, et al., "Tracing Footprints of Femtosecond Laser High-Efficiency Precision 2D/3D Manufacturing Technologies," *Laser & Photonics Reviews* 20 (2026): 03056.

26. D. Pan, S. Liu, J. Li, et al., *Advanced Functional Materials* 31 (2021): 2009386, https://doi.org/10.1002/adfm.202009386.

27. C. Wang, Z. Ye, C. Zhang, et al., *Laser & Photonics Reviews* 19 (2025): 2400708, https://doi.org/10.1002/lpor.202400708.

28. M. Luo, J. Wen, P. Ma, et al., "Three-Dimensional Nanoscale Vortex Line Visualization and Chiral Nanostructure Fabrication of Tightly Focused Multi-Vortex Beams via Direct Laser Writing," *Photonics Research* 12 (2023): 70–77.

29. D. Pan, Z. Fuyang, H. Wang, et al., "Designed 3D Dumpling-Shaped Femtosecond Laser Structured Light Field for Nanoscale Sensing," *Advanced Functional Materials* 34 (2024): 2402323, https://doi.org/10.1002/adfm.202402323.

30. H. Wang, W. Zhang, D. Ladika, et al., "Two-Photon Polymerization Lithography for Optics and Photonics: Fundamentals, Materials, Technologies, and Applications," *Advanced Functional Materials* 33 (2023): 2214211.

31. M. Stavrou, D. Ladika, E. Skliutas, et al., "Direct Measurement of Two-Photon Absorption and Refraction Properties of SZ2080 TM-Based Resists at 515 nm: Insights Into 3D Printing," *Nanophotonics* 14 (2025): 2981–2992, https://doi.org/10.1515/nanoph-2025-0066.

Supporting Information

Additional supporting information can be found online in the Supporting Information section.

Supporting File: lpor71920-sup-0001-SuppMat.docx.